Simulation-derived radar cross sections of a new meteor head plasma distribution model

G. Sugar[1], R. Marshall[2], M. M. Oppenheim[3], Y. S. Dimant[3], and S. Close[1]

[1]Department of Aeronautics and Astronautics, Stanford University, Stanford, California, USA.

[2]Department of Aerospace Engineering Sciences, University of Colorado Boulder, Boulder, Colorado, USA.

[3]Center for Space Physics, Boston University, Boston, Massachusetts, USA.

Key Points:

- We use FDTD simulations to simulate the RCS of different meteor head plasma models derived from an analytical model and PIC simulations
- The radar cross sections off the analytical model and the simulation-derived plasma distributions agree to within 4 dBsm
- The magnetic field orientation with respect to the meteor path has a small effect on the head echo's radar cross section

Corresponding author: Glenn Sugar, gsugar@stanford.edu

This article has been accepted for publication and undergone full peer review but has not been through the copyediting, typesetting, pagination and proofreading process, which may lead to differences between this version and the Version of Record. Please cite this article as doi: 10.1029/2021JA029171.

Abstract

We present results and analysis of finite-difference time-domain (FDTD) simulations of electromagnetic waves scattering off meteor head plasma using an analytical model and a simulation-derived model of the head plasma distribution. The analytical model was developed by Dimant and Oppenheim (`https://doi.org/10.1002/2017JA023960`; `https://doi.org/10.1002/2017JA023963`) and the simulation-derived model is based on particle-in-cell (PIC) simulations presented in Sugar et al. (`https://doi.org/10.1029/2018JA026434`). Both of these head plasma distribution models show the meteor head plasma is significantly different than the spherically symmetric distributions used in previous studies of meteor head plasma. We use the FDTD simulation results to fit a power law model that relates the meteoroid ablation rate to the head echo radar cross section (RCS), and show that the RCS of plasma distributions derived from the Dimant-Oppenheim analytical model and the PIC simulations agree to within 4 dBsm. The power law model yields more accurate meteoroid mass estimates than previous methods based on spherically symmetric plasma distributions.

1 Introduction

As a meteoroid moves through the atmosphere, collisions with atmospheric particles heat the meteoroid surface. Once the surface temperature reaches the sublimation temperature of the meteoroid material, neutral particles will ablate from the surface and experience collisions with atmospheric particles. These collisions can ionize the particles, resulting in a region of plasma surrounding the meteoroid that is orders of magnitude denser than the background ionospheric plasma. High-power large-aperture (HPLA) radars, such as the Jicamarca Radio Observatory, ALTAIR, and the Arecibo Observatory, can detect this high density plasma as signals referred to as meteor head echoes (Chau & Woodman, 2004; Close, 2002; Janches & Revelle, 2005).

HPLA observations of head echoes have been used to estimate meteoroid mass through the equation

$$m = \int \frac{q\mu v}{\beta} dt, \tag{1}$$

where m is the meteoroid mass, q is the electron line density, μ is the meteoroid mass density, v is the meteoroid speed, β is the ionization coefficient defined as the mean number of free electrons produced from ionizing collisions from an ablated meteoroid particle, and the integral is taken over the meteoroid trajectory (Close et al., 2004, 2005;

Campbell-Brown & Close, 2007). The head echo radar cross section (RCS) is converted to q by assuming a plasma density distribution surrounding the ablating meteoroid. Previous studies assume that the plasma distribution is a spherically symmetric Gaussian (Close et al., 2005; Dyrud & Janches, 2008; Campbell-Brown et al., 2012; Zinn et al., 2011). However, this distribution has not been validated with analytical or empirical evidence. Furthermore, the plasma distribution cannot be spherically symmetric because there will be significantly less plasma ahead of the meteoroid compared to behind. Marshall et al. (2017) show that the choice of head plasma distribution can change the estimated meteoroid mass by a factor of 3 for a given RCS. This large source of error motivated the derivation of an analytical model, hereinafter referred to as the Dimant-Oppenheim, or DO model, as well as particle-in-cell (PIC) simulations of an ablating meteoroid (Dimant & Oppenheim, 2017a, 2017b; Sugar et al., 2018, 2019). These new plasma distributions are more realistic models of an actual meteor head plasma because they are physics based models that relax the spherically symmetric Gaussian assumption. The DO model is derived from kinetic theory, while the PIC simulations use a numerical simulation tool commonly used to study plasma physics (Birdsall & Langdon, 2018).

In order to use these improved plasma distributions to estimate meteoroid mass from radar observations, we evaluate the RCS of these plasma distributions using the finite-difference time-domain (FDTD) simulation code used in Marshall and Close (2015). This code has previously been verified and used to determine the RCS of spherically symmetric meteor head plasma distributions in Marshall and Close (2015). We run FDTD simulations of three different types of plasma distributions, the DO model described in Dimant and Oppenheim (2017a, 2017b), a PIC simulation derived model that ignores electric and magnetic fields (referred to as the zero fields simulations) described in Sugar et al. (2018), and a PIC simulation derived model that includes electric fields and either a 0 or 40000 nT background magnetic field (referred to as the electrostatic simulations) described in Sugar et al. (2019). The 40000 nT magnetic field magnitude is within range of reported values at 100 km altitude at mid-latitudes (Chulliat et al., 2015).

2 Simulation Description

The FDTD simulations solve Faraday's Law, Ampere's Law, and a constitutive relation for a cold, collisional, and magnetized plasma:

$$\mu_0 \frac{\partial \overrightarrow{H}}{\partial t} = -\nabla \times \overrightarrow{E}, \tag{2}$$

$$\epsilon_0 \frac{\partial \overrightarrow{E}}{\partial t} = \nabla \times \overrightarrow{H} - \overrightarrow{J}, \tag{3}$$

$$\frac{\partial \overrightarrow{J}}{\partial t} + \nu_e \overrightarrow{J} = \epsilon_0 \omega_p^2 \overrightarrow{E} + \overrightarrow{\omega}_{ce} \times \overrightarrow{J}, \tag{4}$$

where ϵ_0 is the permittivity of free space, $\overrightarrow{E}$ is the electric field, $\overrightarrow{H}$ is the magnetic intensity, $\overrightarrow{J}$ is the current density, μ_0 is the permeability of free space, ν_e is the total electron collision frequency (the sum of the electron-neutral, electron-electron, and electron-ion collision frequencies), ω_p is the electron plasma frequency, and $\overrightarrow{\omega}_{ce}$ is the vector electron gyrofrequency. For a detailed discussion of ν_e, we refer the reader to Section 2.1 of Marshall and Close (2015). The constitutive equation (equation (4)) is derived from the electron momentum equation assuming a cold plasma and a negligible convective term. Equations (2–4) are solved using the FDTD algorithm described in Lee and Kalluri (1999).

The FDTD simulation domain is composed of a 3D Cartesian grid with a convolutional perfectly matched layer boundary condition at each wall (Roden & Gedney, 2000). As shown in Figure 1, the domain is in the meteor's frame of reference with atmospheric particles moving in the $\hat{z}$ direction. In this paper, we assume that the radar's line of sight is aligned with the meteor path, so the incident radar pulse also propagates in the $\hat{z}$ direction. The radar pulse is a linearly polarized (with $\overrightarrow{E}$ oriented 45° from the y-axis in the yz-plane) modulated Gaussian plane wave with a half-power bandwidth $\Delta f = 0.4 f_0$, where f_0 is the radar frequency. Therefore, the radar pulse extends just a few radar wavelengths. For simulations that include a non-zero $\overrightarrow{B}$, the magnetic field lies in the xz-plane.

In order to determine the meteor head plasma RCS, we use a total-field scattered-field (TFSF) formulation and a near-to-far (NTF) field transformation to compute the scattered far fields for a monostatic radar (Inan & Marshall, 2011). The TFSF formulation splits the simulation domain in to an internal total-field (TF) region where most of the electromagnetic scattering takes place, and an external scattered-field (SF) region where negligible scattering occurs. For a detailed discussion on the TFSF formulation and the NTF field transformation, we refer the reader to Chapter 7 and Section 12.4 of Inan and Marshall (2011) respectively.

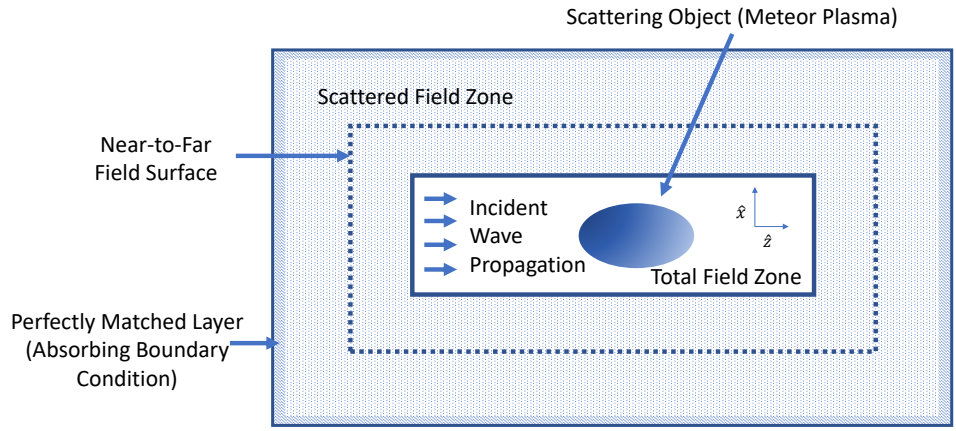

Figure 1. A diagram showing the different parts of the FDTD simulation domain. The incident wave is generated at the total field zone boundary and propagates in the $\hat{z}$ direction. The wave is scattered by the meteor plasma and propagates into the scattered field zone. The near-to-far field surface is inside the scattered field zone and is used to compute the RCS of the scattering object (i.e. the meteor plasma). The entire domain is surrounded with a perfectly matched layer that enforces an absorbing boundary condition.

The plasma distribution models used in this paper provide the ion and/or electron density, but the FDTD simulation equations require the plasma frequency. To convert from particle density to plasma frequency, we use

$$\omega_p = \sqrt{\frac{n_e e^2}{m_e \epsilon_0}}, \tag{5}$$

where n_e is the electron density, e is the elementary charge, m_e is the electron mass, and ϵ_0 is the permittivity of free space. The electrostatic PIC simulations track ions and electrons separately, while the zero field PIC simulations and the DO model assume quasineutrality and keep the ion and electron densities equal to each other. In addition, a background magnetic field, $\vec{B}$, can impact the particle distributions for the electrostatic simulations (Sugar et al., 2019). The magnetic field has no noticeable impact on the ions, but Sugar et al. (2019) showed noticeable effects on the electron distributions. Sugar et al. (2019) also showed regions near the center of the head echo where quasineutrality was violated ($n_e \not\approx n_i$). This is contrary to the DO model which assumes quasineutrality is satisfied throughout the head echo. In order to investigate potential effects of regions

where quasineutrality is violated on RCS, we ran simulations where n_i was used instead of n_e in equation (5) to calculate the plasma frequency.

3 Simulation Parameters

In order to obtain accurate fields in the scattered-field (SF) region of the FDTD simulation domain, the TFSF method requires negligible scattering in the SF region (i.e. $\omega_p/\omega_{\text{radar}} \ll 1$). Over the course of running the FDTD simulations, we found that a plasma frequency three orders of magnitude smaller than the radar frequency in the SF region is sufficient to satisfy this negligible SF region scattering condition. This requirement combined with the finite FDTD simulation domain size establishes an upper limit on the peak plasma frequency of the meteor head plasma distributions that can be used in the FDTD simulations.

When using PIC-derived plasma distributions, the FDTD simulation domain cannot be larger than the original PIC domain without introducing unknown extrapolation errors. This is because the PIC-derived plasma densities are only calculated inside the PIC domain. If we set the FDTD domain size equal to the PIC domain size and set the plasma frequency at each grid cell equal to the PIC results, the $1000\omega_p \leq \omega_{\text{radar}}$ in the SF region condition is not necessarily fulfilled. To ensure that the condition is fulfilled, we scale the PIC-derived plasma frequency at all grid cells such that the maximum ω_p in the SF region equals $\omega_{\text{radar}}/1000$. This results in the maximum plasma frequency in the whole FDTD domain to be approximately $0.56\omega_{\text{radar}}$. Therefore, all FDTD simulations of the electrostatic PIC-derived meteor plasma will be underdense (i.e. $\omega_{p0} < \omega_{\text{radar}}$), the dielectric constant will be greater than 0 for all electrostatic PIC plasma distributions, and they will produce relatively small RCS values compared to overdense plasma distributions where $\omega_{p0}/\omega_{\text{radar}} \geq 1$.

The PIC-derived ω_p values reported in Sugar et al. (2019) can be scaled linearly to correspond to a higher or lower ablation rate. This scaling makes the FDTD simulations computationally feasible for the following reason. The peak plasma densities reported in the electrostatic PIC simulations are approximately 10^{12} m^{-3}, corresponding to $\omega_{p0} = 5.6 \times 10^7$ rad/s, or 9.0 MHz. Using the $\omega_{p0}/\omega_{\text{radar}} \lesssim 0.56$ constraint, we have $\omega_{\text{radar}} \gtrsim 10^8$ rad/s, or 16 MHz. If a 16 MHz incident wave is used with a grid spacing of 0.005 m (the same grid spacing used in the PIC simulations), it requires 3750

grid cells to resolve a single wavelength. This unnecessarily fine spatial resolution results in an unnecessarily small time step, and therefore wasted computation time. The computation time can be decreased by increasing either the grid spacing or ω_{radar}. We do not increase the grid spacing because that would introduce extrapolation errors in the PIC-derived plasma frequencies, so we are left with increasing ω_{radar}. Using a more reasonable grid resolution of 100 grid cells per free space wavelength, which falls in the range of resolutions used in the Marshall and Close (2015) FDTD simulations (50 – 300 grid cells per free space wavelength), a 0.005 meter grid spacing corresponds to a 600 MHz radar frequency. However, this results in little scattering off a plasma with a 9 MHz peak plasma frequency. To satisfy $\omega_{p0}/\omega_{\text{radar}} = 0.56$ with a 600 MHz radar frequency, the ω_{p0} reported in Sugar et al. (2019) must increase by a factor of 37.5, which is accomplished by increasing the ablation rate by a factor of 1406.25. Note that this still satisfies the negligible scattering in the SF region requirement because even though the plasma frequency increased by a factor of 37.5, the radar frequency increased by the same factor (16 MHz to 600 MHz).

Scattering in the SF region is not a significant issue for either the DO model or zero fields PIC-derived distributions. The DO model defines the plasma density at arbitrary distances from the meteor center, so there will not be any extrapolation errors if the FDTD domain size increases. Therefore, the FDTD simulation domain can be made large enough such that the DO model plasma density is sufficiently small (i.e. $1000\omega_p \leq \omega_{\text{radar}}$) inside the SF region even for overdense meteors where $\omega_p > \omega_{\text{radar}}$ in parts of the TF region. While the FDTD domain size for the zero fields PIC-derived plasma is still limited by the PIC domain size, the zero fields PIC domain size can be much larger than the electrostatic PIC domain. This is because unlike the electrostatic PIC simulations, there is no requirement for the zero fields PIC simulation grid to resolve the Debye length, allowing for the zero fields simulations to use a much larger grid spacing and have a much larger domain. The larger domain contains regions farther from the meteor center where there is lower density plasma. The zero fields PIC simulation domain can be sufficiently large to satisfy both an overdense meteor (i.e. $\omega_p > \omega_{\text{radar}}$) in parts of the TF region and the $1000\omega_p \leq \omega_{\text{radar}}$ requirement in the SF region.

Because the FDTD simulation domains using plasma distributions derived from zero fields PIC simulations and the DO model can be large enough to contain overdense meteors while satisfying the low plasma density SF region requirement and the electro-

static PIC simulation derived distributions cannot, we use two different FDTD parameter sets. The first parameter set uses the electrostatic PIC constraints where $\omega_p < \omega_{\text{radar}}$ throughout the entire FDTD simulation domain. Therefore, this parameter set will be referred to as the "underdense parameter set." Note that a naive implementation of the DO model (equation (45) in Dimant and Oppenheim (2017b)) results in a singularity at $r = 0$, resulting in an overdense plasma. However, the DO model plasma density is undefined where r is less than the meteoroid radius. The simulated meteoroids have radii an order of magnitude smaller than a single FDTD grid cell, so the DO model plasma density is undefined at the single grid point associated with $r = 0$. We approximate the DO model plasma frequency at $r = 0$ by setting it equal to the maximum defined plasma frequency in the domain.

The second parameter set has $\omega_p > \omega_{\text{radar}}$ for some region inside the TF region, and will therefore be referred to as the "overdense parameter set." These overdense simulations are able to contain high plasma frequencies in the TF region while satisfying low electromagnetic scattering in the SF region due to much larger domain sizes. All plasma distributions (electrostatic PIC, zero fields PIC, and DO model) are simulated with the underdense parameter set, while only the zero fields PIC and DO model derived distributions are simulated with the overdense parameter set due to the limitations discussed above.

The underdense parameter set values are chosen to maximize the FDTD domain size while not introducing any extrapolation errors when assigning plasma frequency values to the grid. Therefore, we set the FDTD domain volume to equal the electrostatic PIC domain volume used in Sugar et al. (2019). The time step, Δt, is set to satisfy the stability criterion for FDTD simulations containing plasma,

$$\frac{c\Delta t}{\Delta}\sqrt{D} \leq \sqrt{1 - \left(\frac{\omega_{p0}\Delta t}{2}\right)^2} \tag{6}$$

where c is the speed of light, Δ is the grid cell width (assuming $\Delta = \Delta x = \Delta y = \Delta z$), D is the number of simulation spatial dimensions ($D = 3$), and ω_{p0} is the peak plasma frequency in the simulation (Young, 1994). Similar to Marshall and Close (2015), the incident radar frequency is set such that 100 grid cells resolve a wavelength. These and other important parameters for the underdense and overdense parameter set are shown in Table 1.

Parameter	Underdense	Overdense	Units
Grid ($n_x \times n_y \times n_z$)	$512 \times 512 \times 512$	$512 \times 512 \times 512$	cells
Grid Size ($\Delta x = \Delta y = \Delta z$)	0.005	0.15725	m
Radar Frequency (f_{radar})	600	38.15	MHz

Table 1. The values for the FDTD underdense and overdense parameter sets.

The overdense parameter set values are chosen such that 50 grid cells resolve an incident radar frequency of 38.15 MHz, the minimum grid cell per free space wavelength resolution used in Marshall and Close (2015) and the same radar frequency used by the Canadian Meteor Orbit Radar, a radar which we plan to use for evaluating the FDTD results in future work. This coarser grid resolution creates a larger domain compared to the underdense parameter set, enabling the FDTD simulation of overdense meteors while still satisfying the low electromagnetic scattering in the SF region requirement. However, as stated previously, the larger domain makes it impossible to use electrostatic PIC-derived plasma distributions without introducing extrapolation errors by estimating plasma densities outside the PIC domain.

4 Results

This section presents the FDTD simulation results for the meteor head plasma distributions derived from the electrostatic PIC simulations, zero fields PIC simulations, and the DO model. We run FDTD simulations using plasma frequency distributions from 10 different models: 1-4 being electrostatic PIC ion distributions with no magnetic field and a 40000 nT $\overrightarrow{B}$ oriented perpendicular, parallel, and 45° to the meteor path (denoted $\overrightarrow{B}$ $\perp$, $\overrightarrow{B}$ $\parallel$, and $\overrightarrow{B}$ 45° respectively); 5-8 being electrostatic PIC electron distributions with $\overrightarrow{B} = 0$, $\overrightarrow{B}$ $\perp$, $\overrightarrow{B}$ $\parallel$, and $\overrightarrow{B}$ 45°; and 9-10 being zero field PIC distributions and DO model distributions. Figure 2 shows plasma frequency distributions used in the FDTD simulations. We do not show the PIC ion $\overrightarrow{B}$ 45° and $\overrightarrow{B}$ $\perp$ distributions because the ions are not affected by $\overrightarrow{B}$ and those distributions are visually indistinguishable from the PIC ion $\overrightarrow{B} = 0$ distribution.

Figures 3 and 4 show the evolution of $\|\overrightarrow{E}_{\text{tot}}\|^2$, the magnitude squared of the total electric field, and $\|\overrightarrow{E}_{\text{scat}}\|^2$, the magnitude squared of the scattered electric field, for

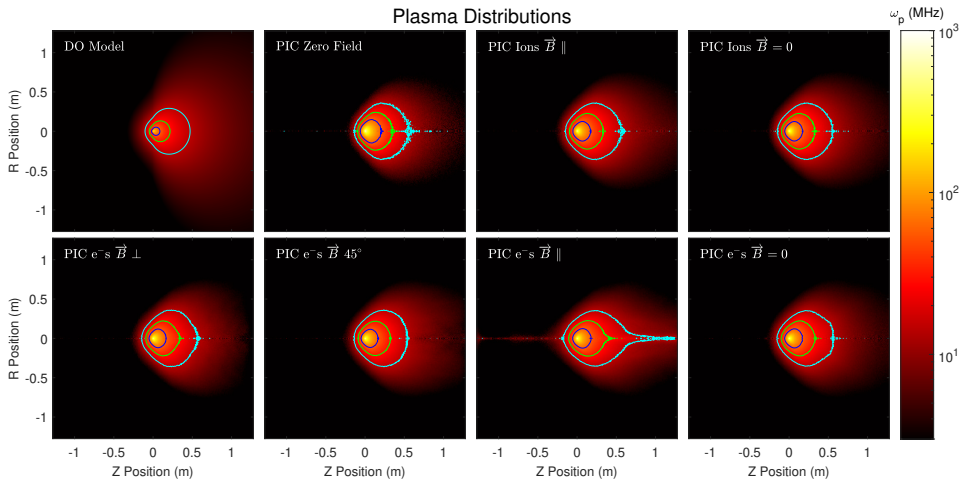

Figure 2. Representative plasma frequency distributions used in the underdense FDTD simulations with contours denoting where ω_p = 15, 30, and 60 MHz in cyan, green, and blue respectively. Starting from the top left image and moving clockwise, the plasma frequency distributions are derived from the particle densities of the DO model, ions from the zero field PIC simulation, ions from the $\vec{B}$ || PIC simulation, ions from the $\vec{B}$ = 0 PIC simulation, electrons from the $\vec{B}$ = 0 PIC simulation, electrons from the $\vec{B}$ || PIC simulation, electrons from the $\vec{B}$ 45° PIC simulation, and electrons from the $\vec{B}$ ⊥ PIC simulation. The ablation rates for each distribution are equal and set such that the peak plasma frequency of the $\vec{B}$ ⊥ PIC simulation is 336 MHz. The plasma frequencies are axially averaged about the meteor path axis ($\hat{z}$), which reduces noise but removes the axial asymmetry that exists in the $\vec{B}$ 45° result.

a typical underdense simulation, specifically the ion distribution of the $\overrightarrow{B} \perp$ electrostatic PIC simulation with $\omega_{p0}/\omega_{\text{radar}} = 0.56$, while Figures 5 and 6 show the evolution of $\|\overrightarrow{E}_{\text{tot}}\|^2$ and $\|\overrightarrow{E}_{\text{scat}}\|^2$ for a typical overdense simulation, specifically the DO model derived distribution where $\omega_{p0}/\omega_{\text{radar}} = 20$. Figures 3-4 and 5-6 are snapshots from movies that are included as supporting information movies 1 and 2 respectively. The incident field can only be seen in the top row of the figures because the bottom rows contain only the scattered field.

Figures 3 and 5 are snapshots when the incident pulse is passing through the meteoroid center and some scattering has already occurred off the front of the head echo, with significantly more scattering appearing in the overdense simulation compared to the underdense simulation. Figures 4 and 6 are snapshots after the incident pulse has moved past the head plasma and show the field being scattered almost uniformly away from the meteor center in both the underdense and overdense simulations. After the incident pulse has passed through the entire simulation domain, significant fields remain in the interior of the head plasma that decay as time progresses. This is a similar phenomenon observed in the Marshall and Close (2015) FDTD simulations. A possible explanation for these fields is that the high-frequency components of the incident pulse are not sufficiently resolved by the FDTD grid resulting in numerical errors. Fortunately, these fields do not radiate outward and reach the NTF surface so they cannot contribute to the meteor plasma's RCS.

4.1 Underdense Scattering

To compare the RCS values of the different plasma distributions, we run multiple FDTD simulations on each distribution using the underdense parameter set with $\omega_{p0}/\omega_{\text{radar}}$ ratios between 0.1 and 0.9. Note that the higher $\omega_{p0}/\omega_{\text{radar}}$ ratios violate the $\omega_{p0}/\omega_{\text{radar}} \lesssim 0.56$ condition, so some scattering outside the TF region may occur for the electrostatic PIC distributions. The radar frequency is fixed at 600 MHz, so we vary ω_{p0} which is equivalent to varying the meteoroid ablation rate since $\omega_p \propto n^2$, and $n \propto C$, where n is the plasma density and C is the ablation rate. Figure 7 shows the RCS vs C for various electrostatic PIC derived distributions, the zero fields PIC derived distribution, and the DO model derived distribution. For the electrostatic PIC distributions, we test both electron (blue) and ion (red) distributions. Because the zero fields PIC distributions and the DO model assume quasineutrality and do not track electrons separately from ions, their

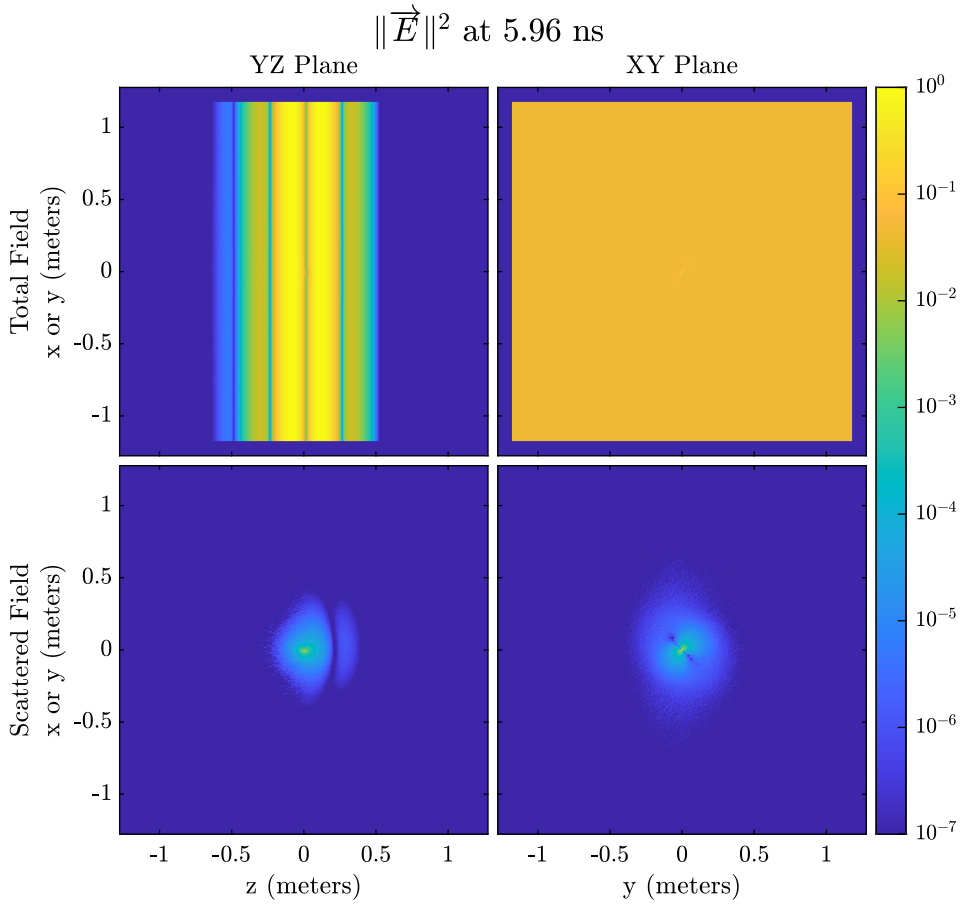

Figure 3. The electric field magnitude squared of the total field (top row) and scattered field (bottom row) in the yz-plane (left column) and xy-plane (right column) when the incident pulse encounters the underdense meteor center using the PIC derived plasma distribution.

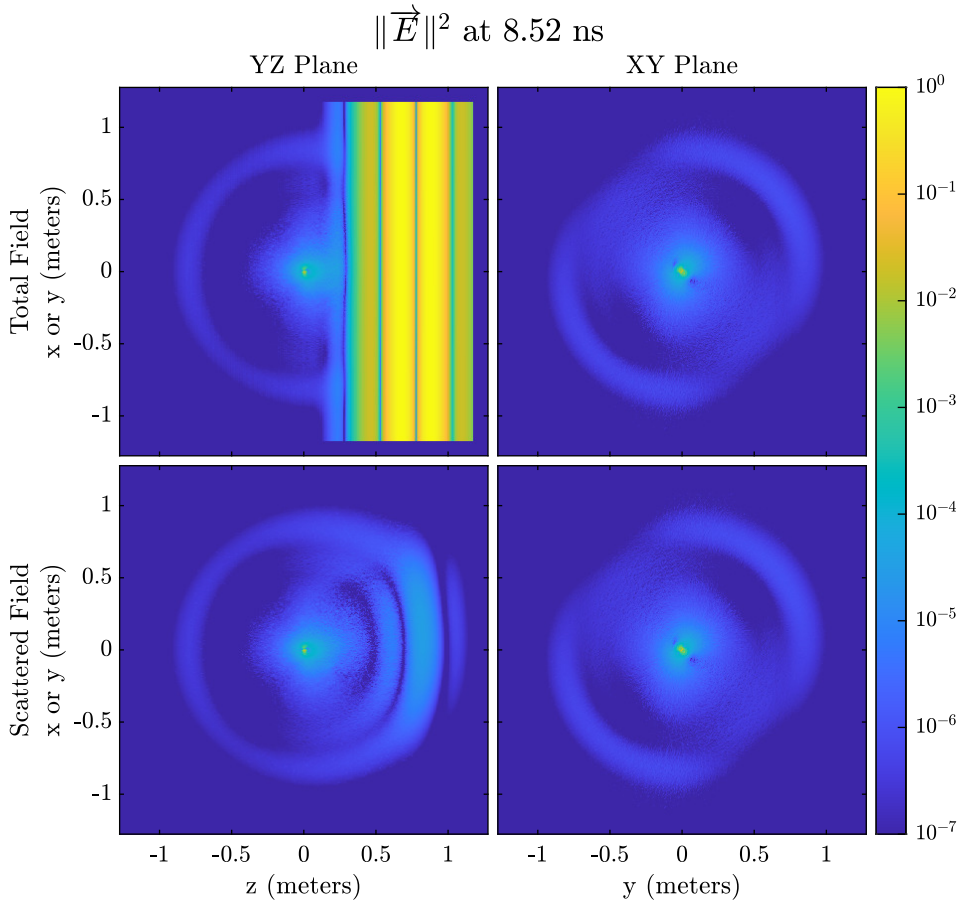

Figure 4. The electric field magnitude squared of the total field (top row) and scattered field (bottom row) in the yz-plane (left column) and xy-plane (right column) after the incident pulse encounters the underdense meteor center using the PIC derived plasma distribution.

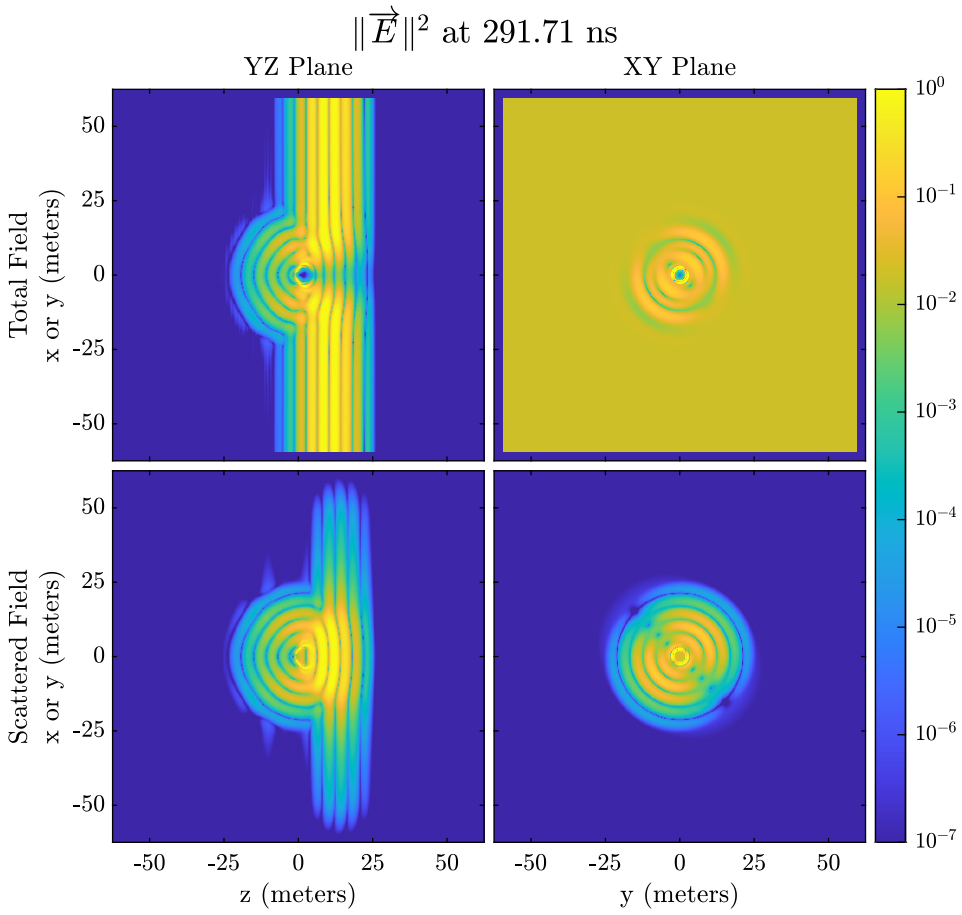

Figure 5. The electric field magnitude squared of the total field (top row) and scattered field (bottom row) in the yz-plane (left column) and xy-plane (right column) when the incident pulse encounters the overdense meteor center using the DO model plasma distribution.

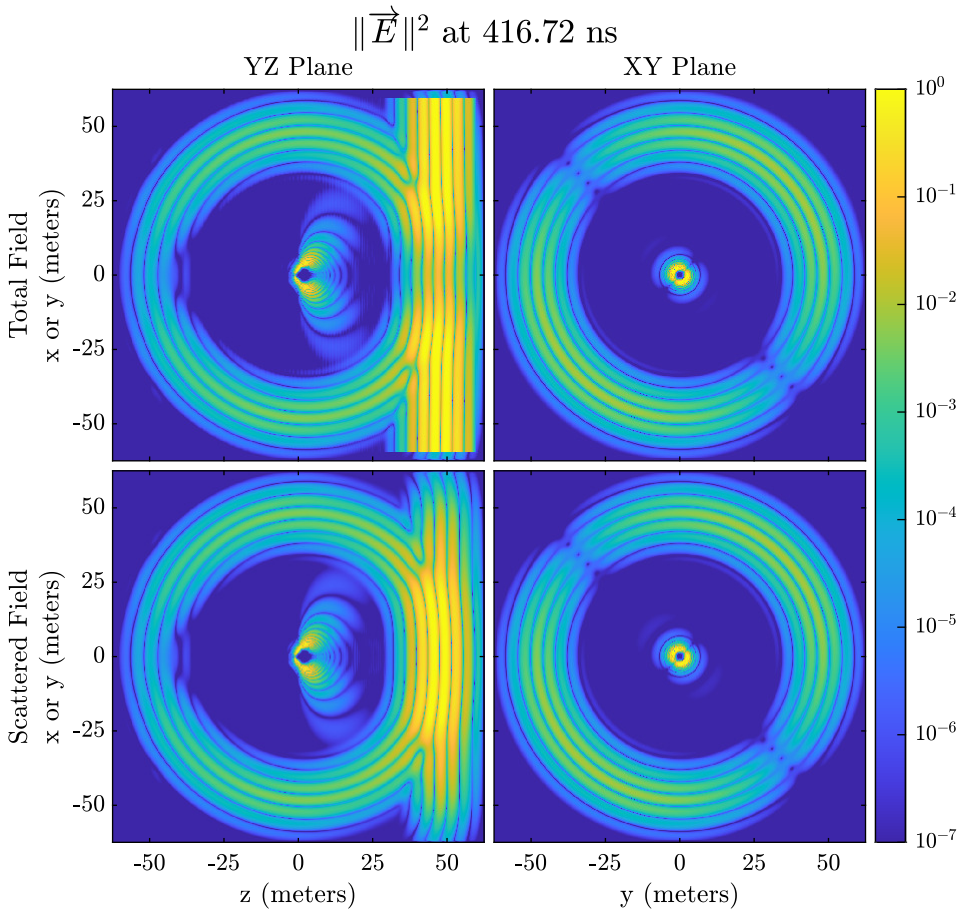

Figure 6. The electric field magnitude squared of the total field (top row) and scattered field (bottom row) in the yz-plane (left column) and xy-plane (right column) after the incident pulse encounters the overdense meteor center using the DO model plasma distribution.

Distribution	a	b	R^2
Electrostatic Ion	1.591×10^{-45}	1.920	0.999867
Electrostatic Electron	5.571×10^{-46}	1.930	0.989057
Zero Fields	1.318×10^{-45}	1.919	0.99995
DO Model	3.408×10^{-45}	1.901	0.999948

Table 2. The parameters for the fitted lines for the underdense FDTD simulations shown in Figure 7 using the equation (8) model and the associated R^2.

data are marked in magenta and black respectively. The different symbols denote which plasma distribution was used in the FDTD simulation. We group each simulation into different types according to the color (electrostatic ion, electrostatic electron, zero fields, and DO model derived distributions) and use the least squares method to fit the data to a power law model

$$S = aC^b, \tag{7}$$

where a and b are the fitting parameters, S (the head echo's RCS) is in units of m^2, and C (the meteoroid ablation rate) is in units of particles/s. Least squares fitting was performed on

$$y = b'x + a', \tag{8}$$

where $y = \log(S), b' = b, x = \log(C)$, and $a' = \log(a)$. The best fit a and b parameters as well as the goodness-of-fit parameter R^2 are shown in Table 2.

Figure 7 and Table 2 show that a power law model, where RCS $\propto C^b$, fits the data well with R^2 values above 0.989 for all plasma distributions. There is a slight shift between the distributions, with the largest difference of about ~ 4 dBsm between the ion and the electron distributions. While the power law model fits all four types of plasma distributions well, the model performs the worst for the electrostatic electron distributions, with an R^2 value of "only" 0.989057 compared to the other 3 distributions which all have $R^2 > 0.9998$. The lower R^2 for the electron distributions is due to fitting the data without regard to the magnetic field orientation. If we separate the electrostatic PIC electron data into subgroups based on the magnetic field orientation and perform fitting, the R^2 values increase to over 0.9995 for each subgroup. The best fit and associated R^2 values for these electron distribution subgroups are shown in Table 3.

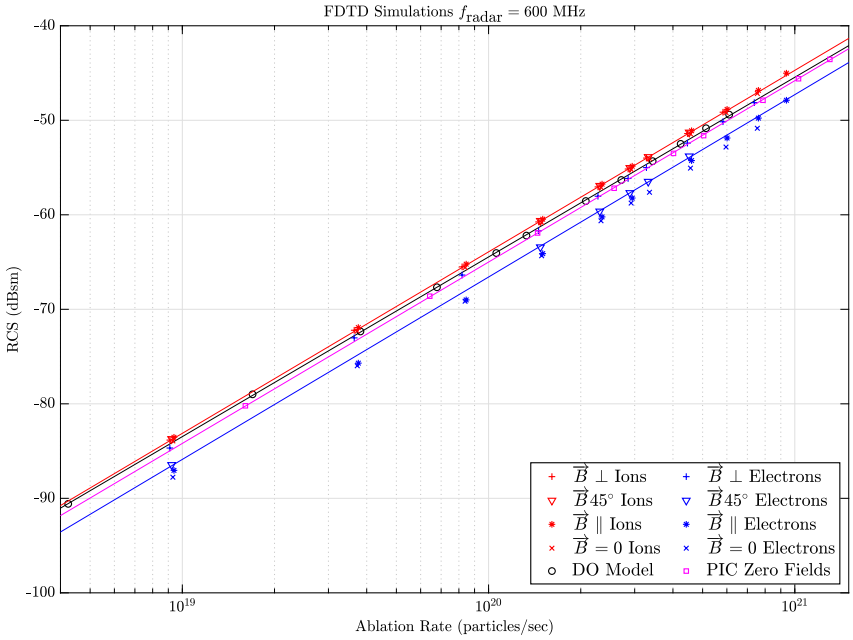

Figure 7. The RCS as a function of meteoroid ablation rate for various underdense plasma distributions. The ion distributions from electrostatic PIC simulations are in red, while electron distributions from electrostatic PIC simulations are in blue. The DO model and zero fields simulations are in black and are denoted with circles and squares respectively. The RCS of electrostatic PIC simulations with varying $\overrightarrow{B}$ are shown. The $\overrightarrow{B}$ $\perp$, $\overrightarrow{B}45°$, $\overrightarrow{B}$ $\parallel$, and $\overrightarrow{B} = 0$ simulations are denoted with $+, \triangledown, \times$, and $*$ respectively. The least squares best fit lines are shown and colored according to the data used for fitting.

The magnetic field clearly affects the electron distribution and RCS, and can change the RCS by up to 4 dBsm. This effect can be explained by noting two phenomena: first, collisions with atmospheric particles will preferentially push particles in the $\hat{z}$ direction (behind the meteoroid); second, electrons are magnetized and will therefore drift faster parallel rather than perpendicular to $\overrightarrow{B}$. When $\overrightarrow{B}$ is aligned with the meteor path, electrons can easily move in the $\hat{z}$ direction. When $\overrightarrow{B}$ is perpendicular to the meteor path, electrons cannot easily move in the $\hat{z}$ direction and therefore there will be a higher electron density in the meteor center. This causes higher plasma frequency gradients, which will increase the scattered field. This phenomenon can be clearly seen in the bottom row of Figure 2, where the $\overrightarrow{B} \parallel$ electron distribution contours are extended farther in the $\hat{z}$ direction than the other distributions.

In the $\overrightarrow{B} = 0$ case, electron motion is no longer constrained by the magnetic field and the RCS is consistently lower than the ion and DO model RCS values. This is likely because electron velocities far exceed ion ones in the PIC simulations. When an ablated particle experiences an ionizing collision in the PIC simulation, the resulting electron and ion will have different velocities. Electrons have higher velocities due to their smaller mass, and therefore diffuse faster than ions. This creates a net positive charge in a region centered around the meteor center where the particle densities and density gradients are largest (Sugar et al., 2019). Outside of this region, the PIC simulations show that quasineutrality holds and ion and electron densities are approximately equal (Sugar et al., 2019). Therefore, for a given electrostatic PIC simulation with no magnetic field, the only significant difference in the ion and electron density distributions is in the region of positive charge near the meteor center where the ions have a higher density and density gradient than the electrons, thus causing the electron-derived distributions to have a smaller RCS than the ion-derived distributions. Figure 7 of Sugar et al. (2019) shows the size of this positively charged region is less than about 1 dimensionless unit equivalent to just 0.08 m for the parameters used in our simulations, which is why the differences in ion and electron densities are not easily noticeable in Figure 2.

If we assume quasineutrality throughout the meteor and use the DO model or PIC ion distributions to calculate plasma frequency, then the magnetic field orientation has a negligible affect on RCS. This is a promising result because it will allow our new meteoroid mass estimation model to be independent of the magnetic field orientation as long as a few dBsm RCS error is acceptable. If a few dBsm error is not acceptable, this er-

Distribution	a	b	R^2
$\overrightarrow{B} \perp$	2.4154×10^{-45}	1.907	0.999961
$\overrightarrow{B} 45°$	6.3407×10^{-46}	1.927	0.999945
$\overrightarrow{B} \parallel$	1.0232×10^{-46}	1.963	0.999593
$\overrightarrow{B} = 0$	4.0359×10^{-46}	1.931	0.999971

Table 3. The parameters and associated R^2 for the best fit lines of the electrostatic PIC electron distributions in Figure 7 grouped by magnetic field orientation using the equation (8) model.

ror can be reduced by relaxing the quasineutrality assumption and conducting a more in depth study on how magnetic field strength and orientation affects the electron distribution and RCS. Such a study is out of the scope of this paper, but it is not necessary for meteors whose path is perpendicular to the magnetic field since their RCS values (blue crosses in Figure 7) are within 1 dBsm of both the DO model and PIC ion-derived distributions.

4.2 Overdense Scattering

We use the overdense parameter set for only the zero fields PIC simulation and DO model derived plasma distributions due to the domain size limitations of the electrostatic PIC simulations. However, it is reasonable to assume that the electrostatic PIC simulation derived ion distributions will produce similar RCS values as the zero fields PIC simulation derived distributions based on the very similar fits of their RCS values in the underdense FDTD simulations (see Figure 7 and Table 2), as well as their similar ion density distributions. We run multiple FDTD simulations on plasma distributions derived from the DO model and the large zero fields PIC simulation with $\omega_{p0}/\omega_{\text{radar}}$ ratios between 1 and 25. Similar to the underdense FDTD simulations in the previous section, we vary ω_{p0} which is equivalent to varying the meteoroid ablation rate. Figure 8 shows the RCS vs ablation rate for the DO model and the zero fields PIC derived distributions as well as the associated best least square fits using the equation (8) power law model. The parameters for the fits and the associated R^2 values are shown in Table 4.

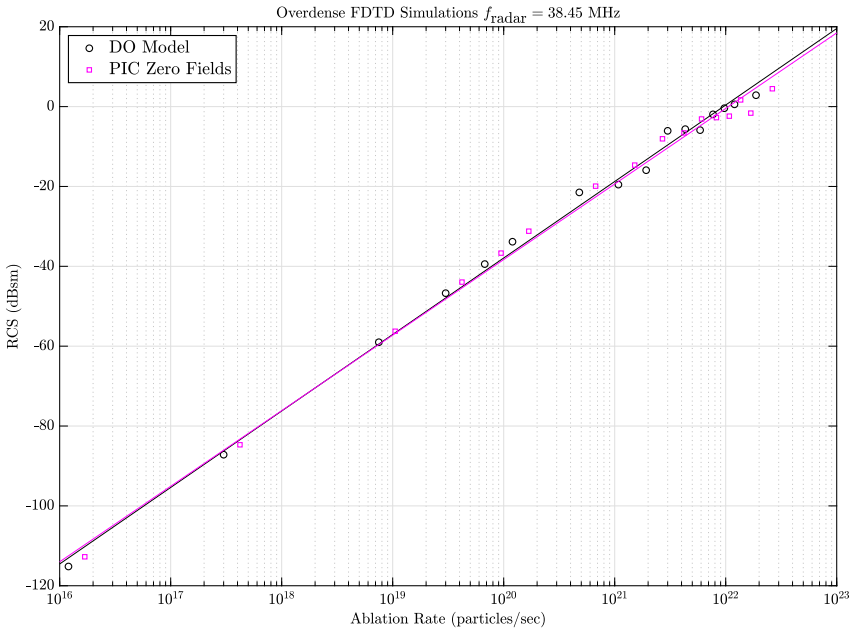

Figure 8. The RCS as a function of meteoroid ablation rate for various overdense plasma distributions. The DO model simulations are in black circles and the zero fields simulations are in magenta squares. The least squares best fit lines are shown and colored according to the data used for fitting.

Distribution	a	b	R^2
Zero Fields	2.087×10^{-42}	1.892	0.994500
DO Model	7.819×10^{-43}	1.916	0.996359

Table 4. The parameters and associated R^2 for the best fit lines associated for the overdense FDTD simulations shown in Figure 8 using the equation (8) model.

Similar to the underdense results, there is very good agreement between the RCS values of the DO model and zero fields PIC distributions. However, there is slightly more error in the best fit power law model in the overdense simulations, with R^2 values under 0.9964 for both the DO and PIC distributions compared to the R^2 values over 0.9998 for the underdense FDTD simulations. One likely explanation is that the overdense simulations cause numerical errors in the FDTD simulation. As the plasma frequency gets higher, especially near the overdense boundary, the dominant propagating electromagnetic field wavelength becomes smaller and eventually becomes smaller than the FDTD grid cell resolution. These wavelengths are not properly resolved, resulting in numerical errors.

5 Discussion and Conclusions

The FDTD simulations reported in this paper are a critical step in developing a more accurate meteoroid mass estimation model that uses radar observations of head echoes. The results show that the RCS can be mapped to a meteoroid ablation rate using a power law model. It is important to note that the RCS to ablation rate models are dependent on the radar frequency (as seen in the different best fit parameters for the underdense and overdense simulations in Tables 2 and 4). There is likely a three degrees of freedom scaling relation between the RCS, radar frequency, meteor peak plasma frequency, and the mean free path of the ablated meteor particles (which is dependent on the altitude and meteor velocity). However, we have not yet fully explored this scaling relationship since we only varied two out of the three degrees of freedom (we kept the ablated particle mean free path constant in all simulations). Once this relationship is quantified, the power law parameters in Tables 2 and 4 should be applicable for meteor observations with different radar frequencies and ablated particle mean free paths. Until then, we caution against using the power law parameters in Tables 2 and 4 to determine meteoroid ablation rate from RCS unless the radar transmits at close to 600 MHz or 38.15 MHz respectively.

The power law dependence of S on the ablation rate C with the exponent $b \approx 2$, as seen in equation (7) and Tables 2-4, can be interpreted in terms of the power law distance dependence of the meteor plasma density around the ablating meteors (Dimant & Oppenheim, 2017b; Sugar et al., 2018, 2019). For the overdense case, the radar backscattered signal can be approximated by assuming the scattering occurs at the surface where

$\omega_p = \omega_{\text{radar}}$. Most of the reflected signal is formed near the location where the radar's line of sight is perpendicular to the reflection surface. With respect to the incident radar wave, this reflection surface is convex and results in the defocusing of the reflected signal. As the curvature radius increases, the defocusing effect decreases and therefore the RCS increases. One might expect that S will be proportional to the square of the curvature radius, which is in turn the order of r_p, the distance of the reflection point to the meteoroid center. This should hold for at least when the radar's line of sight is aligned with the meteor path, which was the orientation of all FDTD simulations presented in this paper.

As discussed in Dimant and Oppenheim (2017b) and Sugar et al. (2018), the plasma density behaves largely as $n \propto C/R$ (with some axial dependence to be ignored here) within an ion-neutral collisional mean free path from the meteoroid center (the near-meteriod region). Assuming the overdense surface lies within this region, we can approximate the overdense region as a sphere with radius r_p and at the sphere's surface we obtain

$$\omega_p^2 = \omega_{\text{radar}}^2 \propto \frac{C}{r_p}. \tag{9}$$

For constant $\omega_p^2 = \omega_{\text{radar}}^2$, the corresponding $S \propto r_p^2 \propto C^2$, which corresponds to equation (7) with $b = 2$. If the overdense surface is situated outside of but not too far from the near-meteoroid region, one might expect a similar $S \propto C^2$ dependence. If the overdense surface is situated far outside the near-meteoroid region, one might still expect a power law dependence but with a different exponent b. However, it is difficult to simulate this case for PIC-derived plasma distributions due to the limited computational domain size.

The power law model for underdense meteors is more difficult to interpret because the backscattered radar signal is no longer formed by a limited region that can be approximated by a single overdense surface but rather the entire meteor head plasma distribution. However, as the ablation rate C increases, the plasma density increases $\propto C$ and the effective backscattered signal-forming size also increases with C. This may result in the net scattered signal to be proportional to approximately C^2, although this statement requires additional studies.

A potentially significant limitation of the power law model is that we assume that the radar's line of sight is aligned with the meteor path. In order to apply the method developed in this work to head echoes with arbitrary orientations with respect to the radar

beam, the incident pulse propagation direction in the FDTD simulation should be oriented appropriately with respect to the meteor path. Another limitation of our model is that we assume all ablated particles originate from a single source and therefore we assume the ablating meteoroid does not fragment. Fragmentation is a phenomenon commonly observed in large meteors that can be observed optically, but is a controversial topic for smaller meteors that can only be detected with radars (Ceplecha et al., 1998). Studies have shown that except for very small or very fast meteoroids, the majority of meteoroid mass loss is due to thermal ablation rather than fragmentation (Vondrak et al., 2008; Rogers et al., 2005). Therefore, it is a reasonable assumption that the majority of meteor head plasma is produced from ionizing collisions between ablated particles originating from the parent meteoroid rather than from a source that previously fractured off the parent meteoroid. However, this model could produce unreliable results when applied to meteoroids that lose significant mass through mechanically induced mass transfer off the surface (i.e. meteoroids with masses $< 10^{-10}$ kg and velocities > 60 km/s). To better predict the RCS of these meteors, one could superimpose multiple DO model distributions offset from each other and run FDTD simulations to investigate the effects of fragmentation. It is also important to note that the DO model and PIC simulations assume the meteoroid size is smaller than the atmospheric mean free path and therefore the method described in this work should not be applied to meteoroids that violate this assumption. An estimate on the meteoroid mass where the model breaks down can be found by noting that HPLA radars observe the majority of meteoroids between 90 and 110 km altitude where the mean free path ranges from about 2 cm to 80 cm (Swarnalingam et al., 2019). Taking the lower bound and assuming a spherical meteoroid with a 2 g/cm^3 density, we find that this model should not be used for meteoroids greater than approximately 8 g.

The final limitation we will address is that determining meteoroid mass using the method outlined in this work requires knowledge of the ionization coefficient β, which is the probability than an ablated particle will experience an ionizing collision. We use the β model derived in Vondrak et al. (2008) in the PIC simulations as well as for calculating the ablation rate of the meteor plasma used in the FDTD simulations. Characterizing β as a function of velocity for different materials is an active topic of research, and it is a relatively trivial task to update this method as better β models are developed since the meteoroid mass is linearly proportional to β in equation (1).

Acknowledgments

This work was supported by NSF Grants AGS-1244842, AGS-1056042, AGS-1755020, AGS-1833209, and AGS-1754895. This work used the Extreme Science and Engineering Discovery Environment (XSEDE), which is supported by National Science Foundation grant number ACI-1548562. The authors acknowledge the Texas Advanced Computing Center (TACC) at The University of Texas at Austin for providing HPC resources that have contributed to the research results reported within this paper. URL: http://www.tacc.utexas.edu. The simulation data and analysis code used to generate all figures and results in this paper are available at Zenodo. URL: https://doi.org/10.5281/zenodo.4514583.

References

Birdsall, C. K., & Langdon, A. B. (2018). *Plasma Physics via Computer Simulation*. CRC press. doi: 10.1201/9781315275048

Campbell-Brown, M. D., & Close, S. (2007, 12). Meteoroid structure from radar head echoes. *Monthly Notices of the Royal Astronomical Society*, *382*, 1309–1316. doi: 10.1111/j.1365-2966.2007.12471.x

Campbell-Brown, M. D., Kero, J., Szasz, C., Pellinen-Wannberg, A., & Weryk, R. J. (2012, 9). Photometric and ionization masses of meteors with simultaneous EISCAT UHF radar and intensified video observations. *Journal of Geophysical Research (Space Physics)*, *117*, A09323. doi: 10.1029/2012JA017800

Ceplecha, Z., Borovička, J., Elford, W. G., Revelle, D. O., Hawkes, R. L., Porubčan, V., & Šimek, M. (1998). Meteor Phenomena And Bodies. *Space Science Reviews*, 327–471. doi: 10.1023/A:1005069928850

Chau, J. L., & Woodman, R. F. (2004, 4). Observations of meteor-head echoes using the Jicamarca 50MHz radar in interferometer mode. *Atmospheric Chemistry & Physics*, *4*, 511–521. doi: 10.5194/acp-4-511-2004

Chulliat, A., Macmillan, S., Alken, P., Beggan, C., Nair, M., Hamilton, B., ... Thomson, A. (2015). *The US/UK World Magnetic Model for 2015-2020: Technical Report* (Tech. Rep.). Retrieved from `https://www.ngdc.noaa.gov/geomag/WMM/data/WMM2015/WMM2015_Report.pdf` doi: 10.7289/V5TB14V7

Close, S. (2002). Scattering characteristics of high-resolution meteor head echoes detected at multiple frequencies. *Journal of Geophysical Research*, *107*(A10), 1295. doi: 10.1029/2002JA009253

Close, S., Oppenheim, M. M., Durand, D., & Dyrud, L. P. (2005, 9). A new method for determining meteoroid mass from head echo data. *Journal of Geophysical Research (Space Physics)*, *110*(A9), 1–6. doi: 10.1029/2004JA010950

Close, S., Oppenheim, M. M., Hunt, S., & Coster, A. (2004, 3). A technique for calculating meteor plasma density and meteoroid mass from radar head echo scattering. *Icarus*, *168*, 43–52. doi: 10.1016/j.icarus.2003.11.018

Dimant, Y. S., & Oppenheim, M. M. (2017a). Formation of plasma around a small meteoroid: 1. Kinetic theory. *Journal of Geophysical Research: Space Physics*, *122*(4), 4669–4696. doi: 10.1002/2017JA023960

Dimant, Y. S., & Oppenheim, M. M. (2017b). Formation of plasma around a small meteoroid: 2. Implications for radar head echo. *Journal of Geophysical Research: Space Physics*, *122*(4), 4697–4711. doi: 10.1002/2017JA023963

Dyrud, L. P. L., & Janches, D. (2008, 9). Modeling the meteor head echo using Arecibo radar observations. *Journal of Atmospheric and Solar-Terrestrial Physics*, *70*(13), 1621–1632. doi: 10.1016/j.jastp.2008.06.016

Inan, U. S., & Marshall, R. A. (2011). *Numerical electromagnetics: The FDTD method*. Cambridge University Press. doi: 10.1017/CBO9780511921353

Janches, D., & Revelle, D. O. (2005, 8). Initial altitude of the micrometeor phenomenon: Comparison between Arecibo radar observations and theory. *Journal of Geophysical Research (Space Physics)*, *110*, A08307. doi: 10.1029/2005JA011022

Lee, J. H., & Kalluri, D. K. (1999). FDTD simulation of electromagnetic wave transformation in a dynamic, inhomogeneous, bounded, and magnetized plasma. *IEEE International Confernece on Plasma Science*, *47*(7), 141. doi: 10.1109/PLASMA.1999.829377

Marshall, R. A., Brown, P., & Close, S. (2017). Plasma distributions in meteor head echoes and implications for radar cross section interpretation. *Planetary and Space Science*, *143*, 203–208. doi: 10.1016/j.pss.2016.12.011

Marshall, R. A., & Close, S. (2015, 7). An FDTD model of scattering from meteor head plasma. *Journal of Geophysical Research (Space Physics)*, *120*, 5931–5942. doi: 10.1002/2015JA021238

Roden, J. A., & Gedney, S. D. (2000, 12). Convolution PML (CPML): An efficient FDTD implementation of the CFS-PML for arbitrary media. *Microwave and*

Optical Technology Letters, *27*(5), 334–339. doi: 10.1002/1098-2760(20001205)27:5⟨334::AID-MOP14⟩3.0.CO;2-A

Rogers, L. A., Hill, K. A., & Hawkes, R. L. (2005, 11). Mass loss due to sputtering and thermal processes in meteoroid ablation. *Planet. Space Sci.*, *53*, 1341–1354. doi: 10.1016/j.pss.2005.07.002

Sugar, G., Oppenheim, M. M., Dimant, Y. S., & Close, S. (2018). Formation of Plasma Around a Small Meteoroid: Simulation and Theory. *Journal of Geophysical Research: Space Physics*, *123*(5), 4080–4093. doi: 10.1002/2018JA025265

Sugar, G., Oppenheim, M. M., Dimant, Y. S., & Close, S. (2019). Formation of plasma around a small meteoroid: Electrostatic simulations. *Journal of Geophysical Research: Space Physics*. doi: 10.1029/2018JA026434

Swarnalingam, N., Janches, D., Carrillo-Sanchez, J. D., Pokorny, P., Plane, J. M. C., Sternovsky, Z., & Nesvorny, D. (2019, May). Modeling the Altitude Distribution of Meteor Head Echoes Observed with HPLA Radars: Implications for the Radar Detectability of Meteoroid Populations. *The Astronomical Journal*, *157*(5), 179. doi: 10.3847/1538-3881/ab0ec6

Vondrak, T., Plane, J. M., Broadley, S., & Janches, D. (2008). A chemical model of meteoric ablation. *Atmospheric Chemistry and Physics*, *8*(23), 7015–7031. doi: 10.5194/acp-8-7015-2008

Young, J. L. (1994). A full finite difference time domain implementation for radio wave propagation in a plasma. *Radio Science*, *29*(6), 1513–1522. doi: 10.1029/94RS01921

Zinn, J., Close, S., Colestock, P. L., MacDonell, A., & Loveland, R. (2011, 4). Analysis of ALTAIR 1998 meteor radar data. *Journal of Geophysical Research (Space Physics)*, *116*, A04312. doi: 10.1029/2010JA015838